



## Lubrication effects on magmatic mush dynamics

Alexandre Carrara<sup>a,\*</sup>, Alain Burgisser<sup>a</sup>, George W. Bergantz<sup>b</sup>

<sup>a</sup> Univ. Grenoble Alpes, Univ. Savoie Mont Blanc, CNRS, IRD, IFSTTAR, ISTERre, 38000 Grenoble, France

<sup>b</sup> Department of Earth and Space Sciences, Box 351310, University of Washington, Seattle, WA 98195, USA

### ARTICLE INFO

#### Article history:

Received 5 December 2018

Received in revised form 5 May 2019

Accepted 8 May 2019

Available online 16 May 2019

#### Keywords:

Magma rheology

Crystal mush

Multiphase physics

Dense suspensions

CFD-DEM

### ABSTRACT

Silicic magma bodies are formed by repeated injections of mobile magma and reside as a crystal-rich mush. Numerical studies of open-system events have revealed the complexity of mixing and rheological behavior. This is associated with the dilation of the crystal network and the possible occurrence of a lubricated regime. Lubrication forces are hydrodynamic interactions occurring when neighboring crystals have relative motion. The effect of such dissipative forces has not yet been explored in the case of magmatic mush. Here, we investigate the effects of lubrication on mush dynamics and on magma transport. First, we propose scaling relationships to assess the relative importance of the forces controlling the motion of one crystal within a mush by adding lubrication terms into the Basset-Boussinesq-Oseen equation that describes crystal motion in a viscous melt. We then investigate lubrication effects at the macroscopic scale with computational fluid dynamics with discrete element modeling (CFD-DEM) simulations that include these forces. We explore two cases: crystal mush sedimentation and the injection of a crystal-free magma inside a mush. We perform all simulations twice, with and without lubrication forces, and compare the results. At the grain scale, we show that three dimensionless numbers and the crystal content can describe the competition between viscous drag, buoyancy, and lubrication. Two of these numbers (Stokes and Froude numbers) have been previously employed in the context of dilute suspensions. The third is a new form of the Sommerfeld number that measures the importance of lubrication. At the macroscopic scale, simulation pairs (with and without lubrication forces) exhibit very similar behavior when in steady state. The duration of the transient regime preceding steady state, however, is increased when lubrication forces are included. Lubrication causes an apparent bulk strain hardening followed by softening at the initiation of the mush motion. Our results show that lubrication opposes dilation and the initiation of motion within the magmatic mush during this transient phase. Our results highlight the control that the crystal network exerts on magma transport and provide a novel way to evaluate when lubrication matters.

© 2019 Elsevier B.V. All rights reserved.

### 1. Introduction

Magma bodies residing in the crust are formed by repeated injections of mobile magma and are inferred to reside in a mushy state (Bachmann and Bergantz, 2004; Cashman et al., 2017; Hildreth, 2004). A mush is magma with a high concentration of crystals (also called particles here). The rheology of mushes is one of most critical phenomenon controlling magma transport within volcanic systems (Caricchi et al., 2007; Cordonnier et al., 2012; Kendrick et al., 2013; Lavallée et al., 2012, 2007; Ryerson et al., 1988; Sparks, 2003), sometimes influencing eruptive styles (Karlstrom et al., 2012). However the transition between a mobile magma and the mush state is complex and poorly understood. Macroscopically, this transition is characterized by the emergence of non-Newtonian behaviors characterized by shear thinning and possibly

continuous and/or discontinuous shear thickening (Lavallée et al., 2012, 2007; Petford, 2009; Mader et al., 2013 and references therein).

However, attempts to index crystal-rich rheology to the volume fraction of crystals, whether by a Krieger-Dougherty type power law or by a viscous number scaling relation (Bergantz et al., 2017), fail to recover non-Newtonian behavior in the absence of inertia. These models can predict the correct volume fraction dependence at a fixed shear rate, but cannot capture shear rate dependence at fixed volume fraction (e.g., Mari et al., 2014). This is because there is only one stress scale associated with the Krieger-Dougherty relation: the one associated with hydrodynamics. And while the viscous number framing includes a gravitational stress scale, it cannot predict the transition to discontinuous shear thickening or differentiate between jamming occurring from steric or frictional effects. It is now apparent that these non-Newtonian processes arise by the initiation of normal and frictional tangential forces from particle contact, which can happen at particle volume fractions of 0.3 or less. The onset of friction introduces an additional stress scale into the rheology that is not resolved in the traditional framing.

\* Corresponding author.

E-mail address: [carrara.alexandre.univ@gmail.com](mailto:carrara.alexandre.univ@gmail.com) (A. Carrara).

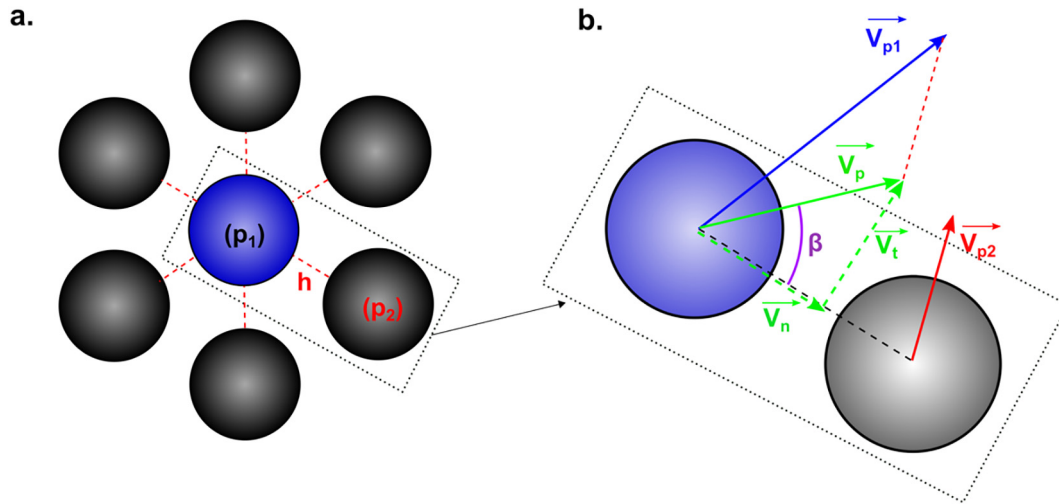


**Fig. 1.** Conceptual model considered to scale the importance of lubrication forces. [A] The central target particle ( $p_1$ ) is in blue. Its six neighboring particles are indicated in black and are arranged in a hexagonal lattice. The minimum distance between the edges of particles pairs is indicated by red dashed lines and has been exaggerated for clarity. The black dashed box represents the region depicted in B. [B] Zoom on a particle pair. The blue particle represents the particle  $p_1$  and the black one represents  $p_2$ . Their velocity vectors are represented by blue and red arrows, respectively. The green arrow represents the relative particle velocity seen by particle  $p_1$ ,  $\vec{v}_p$ . The two dashed green arrows indicate the decomposition of the relative velocity in its normal,  $\vec{v}_n$ , and tangential,  $\vec{v}_t$ , components. The angle between the vectors  $\vec{v}_p$  and  $\vec{v}_n$ , is called the incidence angle  $\beta$  (purple).

Hence any process that influences the onset of frictional contacts, such as lubrication, can have a profound effect on the rheology of the mush.

Following Bergantz et al. (2017), we further develop the scaling relationships for lubrication with an emphasis on how lubrication influences the time-dependence of a system as it moves between locked or frictional states. When neighboring particles graze each other in a viscous fluid, the ensuing hydrodynamic interactions create tangential lubrication forces on the particles (Jeffrey and Onishi, 1984; Marzougui et al., 2015). Normal lubrication forces arise when particles approach or are separated from each other. In sheared suspensions, lubrication effects due to these two forces dominate over that caused by particle spinning (Marzougui et al., 2015). The relative motions required to squeeze or suck the fluid from the gap between their edges result in the dissipation of the particle kinetic energy, which depends mostly on the fluid viscosity and particle separation distance. The importance of lubrication forces on mush dynamics is not obvious because these forces can be viewed as either opposing, or promoting the fluidization of the dense suspension in response to the arrival of new magma (Bergantz et al., 2017). Lubrication also influences the path of individual crystals during remobilization and the time they have to respond to changes in their chemical environment. As a result, the residence time of crystals within magmatic systems is affected by the transient lubricated state, the effects of which cannot be ignored when reconstructing the thermal history of crystals (e.g., Cooper and Kent, 2014; Barboni et al., 2016).

Here we use computational fluid dynamics with discrete element modeling (CFD-DEM) to explore the role of lubrication in mush systems. CFD-DEM numerical simulations have proven to be a powerful tool to study magmatic mush dynamics (Bergantz et al., 2017, 2015; Schleicher et al., 2016). In such models, the behavior of the continuous fluid phase (silicate melt) is computed by solving Navier-Stokes equations on an Eulerian grid. Individual crystals are represented by spheres, the trajectories of which are computed in a Lagrangian framework with the Newton laws of motion. This representation of the solid phase allows the CFD-DEM framework to explicitly resolve solid/solid interactions such as contact and friction and the coupling with the surrounding fluid. Despite high computational costs, models based on CFD-DEM have been validated (Deen et al., 2007) and are often employed as benchmarks to validate other numerical approaches (e.g. Chen and Wang, 2014). Previous CFD-DEM models used to study mush dynamics include the micro-scale physics of contact, drag, and

buoyancy forces (Bergantz et al., 2017, 2015; McIntire et al., 2019; Schleicher et al., 2016) but do not explicitly consider lubrication forces.

Our objective is to address the effects and importance of lubrication forces on the dynamic of magmas and mushes. We first propose a scaling of the relative importance of lubrication forces at the particle scale with a simplified expression of lubrication. We then focus on macroscopic scale dynamics by investigating with CFD-DEM simulations the effects of a more complete description of lubrication in two canonical cases of fluid dynamics relevant to magmatic systems, the sedimentation and the remobilization of a dense particle bed. Finally, the effect of lubrication forces on magma and mushes dynamics is discussed.

## 2. Method

### 2.1. Formulation of the BBO equation with lubrication forces

To scale the importance of lubrication forces on a dense granular suspension, we consider a system of smooth spheres arranged in a hexagonal lattice and immersed in a viscous fluid with a density contrast (i.e.  $\rho_p \neq \rho_f$ , where  $\rho_p$  is the sphere density and  $\rho_f$  is the fluid density) (Fig. 1 A; symbols are summarized in Table 1). The particles have the same diameter,  $d_p$ , and they are separated by a small but finite distance,  $h$ . The motion of a given particle in a magmatic viscous fluid can be described by the truncated Lagrangian Basset-Boussinesq-Oseen (BBO) equation (Bergantz et al., 2017). Following Marzougui et al. (2015), we neglect lubrication effects arising from rolling and twisting relative motions between the particles, which only produce marginal effects compared to normal and tangential lubrication (Fig. 10 in Marzougui et al., 2015). There are different formulations of the lubrication forces. At the particle scale, we use a simplification proposed by Marzougui et al. (2015) of the more complete expression of Jeffrey and Onishi (1984) because it is amenable to algebraic manipulations. In the CFD-DEM model (Section 2.2), we use the formulation of Frankel and Acrivos (1967) because it does not feature the unphysical negative torques at large inter-particle distance of the particle-scale expression (Marzougui et al., 2015). Incorporating both normal<sup>1</sup> and tangential

<sup>1</sup> In Bergantz et al. (2017), the normal lubrication expression should be replaced by the form used here (Eqs. (1) and (3) with  $\beta = 0$ ) to take into account that contacts occur between two spheres and not between a sphere and a plate (Andreotti et al., 2013).

**Table 1**  
List of variables and their meaning.

Variable (unit)	Definition
$A$	Lubrication parameter
$C$	Particle shape and roughness parameter
$d_p$ (m)	Particle diameter
$e_n; e_t$	Normal and tangential restitution coefficients
$F_R$	Froude number
$g$ (m s <sup>-2</sup> )	Gravitational acceleration
$h$ (m)	Distance between particle edges
$j$	Ratio of the distance between particle edges and their radius
$S_T$	Stokes number
$S_o$	Sommerfeld number
$t$ (s)	Time
$U_{inj}$ (m s <sup>-1</sup> )	Injection velocity
$U_{mf}$ (m s <sup>-1</sup> )	Minimum fluidization velocity
$U_T$ (m s <sup>-1</sup> )	Particle terminal velocity
$v_{p_i}$ (m s <sup>-1</sup> )	$i$ th particle velocity
$v_p$ (m s <sup>-1</sup> )	Relative velocity between two particles
$v_f$ (m s <sup>-1</sup> )	Relative velocity between particle and fluid
$v_{fluid}$ (m s <sup>-1</sup> )	Fluid velocity
$v_0$ (m s <sup>-1</sup> )	Fluid characteristic velocity
$W$ (m)	3rd dimension length
$\delta$ (m)	Fluid characteristic distance
$\alpha$	Permeability parameter
$\beta$ (°)	Incidence angle
$\Delta\rho$ (kg m <sup>-3</sup> )	Density contrast between fluid and particles
$\varepsilon$ (m)	Particle roughness
$\eta_f$ (Pa s)	Fluid viscosity
$\rho_p$ (kg m <sup>-3</sup> )	Particle density
$\rho_f$ (kg m <sup>-3</sup> )	Fluid density
$\tau; \tau_d; \tau_l$ (s)	Characteristic times
$\Phi$	Particle volume fraction
$\Phi_{max}$	Particle maximum packing fraction

lubrications forces, the BBO equation can be expressed as:

$$\frac{d \vec{v}_{p1}}{dt} = \frac{\Delta\rho \vec{g}}{\rho_p} - \frac{3 \eta_f v_f}{2 \alpha \rho_p d_p^2} - \frac{3 \eta_f \vec{v}_p}{\rho_p d_p^2} A \quad (1)$$

where  $\vec{v}_{p1}$  is the particle velocity,  $\Delta\rho = \rho_p - \rho_f$ ,  $\eta_f$  is the fluid viscosity,  $t$  is the time, and  $\vec{g}$  is the gravitation acceleration. The left-hand side of Eq. (1) represents the acceleration of the particle considered and the first term on the right-hand side is the reduced buoyancy. The second term corresponds to the viscous drag exerted by the fluid on the particle due to the velocity difference between the particle and the surrounding fluid,  $\vec{v}_f = \vec{v}_{p1} - \vec{v}_{fluid}$ . The coefficient  $\alpha$  refers to the permeability of the dense particle network, which is given by the Carman-Kozeny relationship (Bergantz et al., 2017):

$$\alpha = \frac{(1-\Phi)^3}{C \Phi^2} \quad (2)$$

where  $\Phi$  is the particle volume fraction and  $C$  is a constant depending on particle shape and roughness ( $C = 44.4$  for smooth sphere, MacDonald et al., 1991). As pointed out by Bergantz et al. (2017) this drag law is only reliable for dense suspensions when  $\alpha > 1/12$ , which corresponds to  $\phi > \sim 0.3$ . The last term on the right-hand side of Eq. (1) incorporates both normal and tangential lubrications forces due to the relative velocity between the particle and its neighbor (subscripts  $p1$  and  $p2$  respectively),  $\vec{v}_p = \vec{v}_{p1} - \vec{v}_{p2}$ . The relationship between normal and tangential forces is expressed in the  $A$  coefficient (Marzougui et al., 2015):

$$A = \frac{3 \cos(\beta)}{2j} - \ln(j) \sin(\beta) \quad (3)$$

where  $j$  is the ratio of the distance between the particle edges,  $h$ , over their diameter ( $j = 2h/d_p$ ), and  $\beta$  is the incidence angle that corresponds

to the angle between the relative velocity and the vector linking the particle pair centers (Fig. 1 B). In a hexagonal lattice,  $j$  can be linked to the ratio of the particle volume fraction over the maximum packing fraction (Ancey et al., 1999):

$$j = 1 - \left( \frac{\Phi}{\Phi_{max}} \right)^{\frac{1}{3}} \quad (4)$$

The tangential lubrication force expression used in Eqs. (1) and (3) gives reliable results up to  $j = 0.2$  (Fig. 3 in Marzougui et al., 2015). As a result, Eq. (1) is valid from  $\Phi/\Phi_{max} < 1$  down to  $\Phi/\Phi_{max} = 0.5$ , which corresponds to  $j = 0.2$ . For a system of two particles (Fig. 1 B), the meaning of the incidence angle,  $\beta$ , is obvious and decomposes the relative velocity vector into normal and tangential components. For a multiparticle system (Fig. 1 A), each particle pair displays a different relative velocity and incidence angle with respect to the central particle. The motion of the central particle is affected by the resultant lubrication force caused by all neighboring particles, which means that  $\vec{v}_p$  and  $\beta$  must be viewed as representative relative particle velocity and incidence angle, respectively. The meaning of these two parameters in a multiparticle system is explored in the supplementary material SIB.

## 2.2. CFD-DEM model

We performed CFD-DEM numerical simulations by using the MFIX software (<https://mfix.netl.doe.gov/>). The equations are summarized in the supplementary material SIA. Detailed explanations about the theory and implementation of the model can be found in Garg et al. (2010), Syamlal (1998), Syamlal et al. (1993), and validation of the DEM approaches in Garg et al. (2012) and Li et al. (2012). We included both normal and tangential lubrication forces into the model by implementing the formulas used by Marzougui et al. (2015). We emphasize that the drag and lubrication expressions used in the simulations are different from those used for in the scaling approach (i.e. the tangential lubrication force in Table A1 is the expression of Frankel and Acrivos (1967) and not that of Eqs. (1) and (3)) to ensure the consistency of the DEM modeling in dilute conditions.

Unfortunately, no simple analytical solution of the approach of two spheres exists because both  $\vec{v}_p$  and  $h$  that appear in the lubrication force vary with time. We validated instead our implementation of the lubrication forces by reproducing the particle bouncing experiment from Gondret et al. (2002). We obtain a good fit between the experimental results and our numerical simulation. Details and results of this validation are reported in the supplementary materials SIC.

## 3. Results

### 3.1. Grain scale

#### 3.1.1. Scaling of the relative importance of the forces exerted on a particle

To determine what parameters control most particle motion, we express the vectors involved in Eq. (1) by their magnitudes, which are always positive by definition. This allows us to quantify what are the dominant forces among buoyancy, viscous drag and lubrication. The importance of gravitational forces can be expressed by using the terminal fall velocity of the particle, which combines several variables involved in Eq. (1):

$$U_T = \frac{\Delta\rho g d_p^2}{3 \eta_f} \quad (5)$$

We introduce  $U_T$  in the drag and lubrication terms by multiplying each term by  $1 = U_T/U_T = (\Delta\rho g d_p^2)/(3 \eta_f U_T)$ . After rearranging, Eq. (1)

becomes:

$$\frac{\rho_p}{\Delta\rho g} \frac{d v_{p1}}{dt} = 1 - \frac{v_f}{2\alpha U_T} - \frac{A v_p}{U_T} \quad (6)$$

The left-hand side of Eq. (6) represents the non-dimensional gravitational acceleration of the particle (p1). The first term on the right-hand-side of Eq. (6) that equals unity expresses the fact that the gravitational acceleration of the particle is constant in time. The two last terms represents the non-dimensional drag and lubrication forces, respectively. The equality between drag and buoyancy forces occurs when  $1 = v_f/(2\alpha U_T)$ , which implies that:

$$v_f = 2\alpha U_T \quad (7)$$

Similarly, the balance between buoyancy and lubrication is expressed by the equality  $1 = A v_p/U_T$ , which yields:

$$v_p = \frac{U_T}{A} \quad (8)$$

Finally, equality between the drag and lubrication forces requires that  $v_f/(2\alpha U_T) = A v_p/U_T$ , which yields the following relationship between  $v_p$  and  $v_f$ :

$$v_f = 2\alpha A v_p \quad (9)$$

The three forces balance each other when  $\frac{v_f}{2\alpha U_T} = 1$  and  $\frac{A v_p}{U_T} = 1$ . Thus Eq. (7) is valid for  $\frac{A v_p}{U_T} \leq 1$ , Eq. (8) is valid for  $\frac{v_f}{2\alpha U_T} \leq 1$ , and Eq. (9) is valid for  $\frac{A v_p}{U_T} \geq 1$  and  $\frac{v_f}{2\alpha U_T} \geq 1$ .

The three force domains and associated boundaries are summarized in Fig. 2. Predicting which forces control the motion of a particle requires to replace that particle in the force diagram. Its position depends

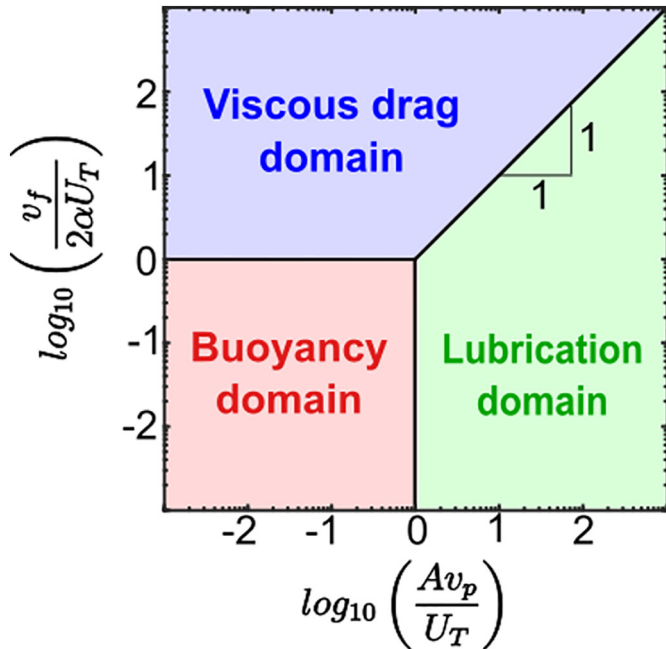


**Fig. 2.** Force diagram summarizing scaling results. Axes have logarithmic scales with the ratios  $A v_p/U_T$  as abscissa and  $v_f/2\alpha U_T$  as ordinate. The red, blue and green areas correspond to the domains where buoyancy, drag and lubrication dominate, respectively. Boundaries between the domains are reported with black lines corresponding to Eqs. (7)–(9), respectively. Boundaries meet at a point where all forces have the same importance on particle motion.

on the ratio  $\Phi/\Phi_{max}$ , the angle  $\beta$ , and the two relative velocities  $v_p$  and  $v_f$ . The two first variables form the  $\alpha$  and  $A$  coefficients. The influence of lubrication forces is maximum when the coefficient  $A$  is maximized, which means that it is possible to define an optimal angle,  $\beta_{opt}$ , that most promotes lubrication. This angle depends also on  $\Phi/\Phi_{max}$  and it corresponds to the point at which the derivative of  $A$  with respect to  $\beta$  is null:

$$\beta_{opt} = \tan^{-1}\left(-\frac{2j \ln(j)}{3}\right) \quad (10)$$

Conversely, we found that  $\beta = 90^\circ$  is most adverse to lubrication effects, which corresponds to pure tangential relative motion.

### 3.1.2. Dimensionless formulation

The dimensionless form of Eq. (1) is (see Supplementary material SID):

$$\frac{d\tilde{v}_{p1}}{d\tilde{t}} = \frac{1}{F_R^2} \frac{\tilde{v}_f}{S_T} - \frac{\tilde{v}_p}{S_O} \quad (11)$$

The three velocities  $\tilde{v}_{p1}$ ,  $\tilde{v}_f$ , and  $\tilde{v}_p$  correspond to the dimensionless forms of the velocities involved in Eq. (1) that are defined as  $\tilde{v}_{p1} = v_{p1}/v_0$ ,  $\tilde{v}_f = v_f/v_0$  and  $\tilde{v}_p = v_p/v_0$ , where  $v_0$  is the characteristic speed. The variable  $\tilde{t}$  is the dimensionless time defined as  $\tilde{t} = t/\tau$ , where  $\tau$  is the characteristic time corresponding to the ratio of the characteristics length,  $\delta$ , and speed,  $v_0$  ( $\tau = \delta/v_0$ ). The three terms  $F_R$ ,  $S_T$  and  $S_O$ , are the dimensionless Froude, Stokes and Sommerfeld numbers, respectively. Both  $F_R$  and  $S_T$  were used previously by Burgisser et al. (2005) and Bergantz et al. (2017) to scale the controls of buoyancy and drag forces, respectively, and are expressed here as:

$$S_T = \frac{2\alpha \rho_p d_p^2 v_0}{3 \eta_f \delta} = \frac{\tau_d}{\tau}$$

$$F_R^2 = \frac{\rho_p v_0^2}{\Delta\rho g \delta} \quad (12b)$$

The Stokes number characterizes the viscous drag coupling between the particle and the surrounding fluid, which corresponds to the ratio between the drag particle relaxation time ( $\tau_d = d^2 \rho_p/6 \alpha \eta_f$ ) and the characteristic time ( $\tau = \delta/v_0$ ). The Sommerfeld number characterizes the importance lubrication forces, and expresses the ratio between the lubrication particle relaxation time  $\tau_l$  ( $\tau_l = A d^2 \rho_p/3 \eta_f$ ) and  $\tau$ :

$$S_O = \frac{\rho_p d_p^2 v_0}{3 \eta_f A \delta} = \frac{\tau_l}{\tau}. \quad (13)$$

In the context of dense suspensions, the most appropriate characteristic distance is the gap between the particle edges,  $h$ . The relevant characteristic speed  $v_0$  depends on the nature of the external forcing applied to the system. It could be, for instance, an externally imposed shear rate expressed as  $v_0/h$ .

## 3.2. Macroscopic scale

### 3.2.1. Experiment 1: Rayleigh–Taylor instabilities

The first numerical experiment consists of a particle bed initially in a jammed state at the top of a tank filled with a viscous fluid. Simulations use non slip boundary conditions at the walls. The bed is initially at rest and simulations start when gravity is switched on. Due to the negative buoyancy of the particles, Rayleigh–Taylor-type instabilities are generated as shown by experimental (Michioka and Sumita, 2005) and numerical (Bergantz and Ni, 1999) experiments. To look at the effects of lubrication forces at the macroscopic scale of the settling bed, we

**Table 2**

Parameters used for the Rayleigh–Taylor instabilities experiment. The value of normal and tangential restitution coefficient is the same between simulations 1A and 1B. These two values are artificially decreased to  $e_n = 0.01$  and  $e_t = 0.005$  in simulation 1C in an attempt to reproduce the effect of lubrication forces (see Supplementary materials).

Run	$\eta_f$ (Pa s)	$d_p$ (m)	$\rho_p$ (kg m <sup>-3</sup> )	$\rho_f$ (kg m <sup>-3</sup> )	Bed dimension (m × m)	$e_n$	$e_t$	Lubrication
1A	0.2	$2.5 \pm 0.2 \cdot 10^{-4}$	2500	1250	$0.03 \times 0.005$	0.7	0.35	Yes
1B	0.2	$2.5 \pm 0.2 \cdot 10^{-4}$	2500	1250	$0.03 \times 0.005$	0.7	0.35	No
1C	0.2	$2.5 \pm 0.2 \cdot 10^{-4}$	2500	1250	$0.03 \times 0.005$	0.01	0.005	No

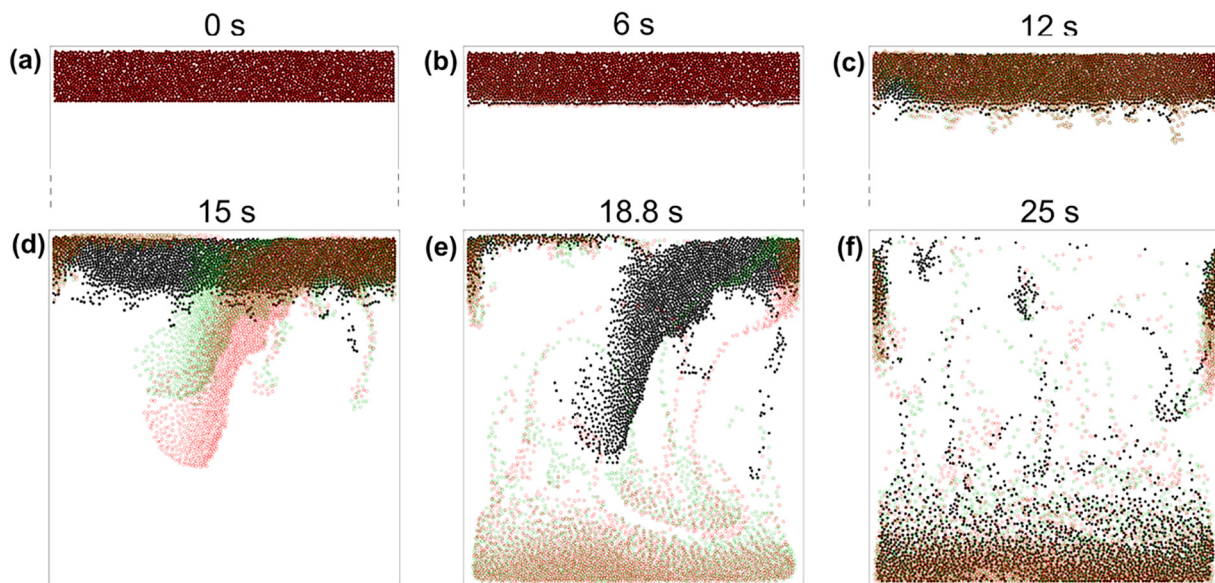
performed the same simulation twice, once taking lubrication forces into account (simulation 1A) and once without lubrication forces (simulation 1B). A third simulation (simulation 1C) was run without lubrication forces but mimicking lubrication by setting a low restitution coefficient (ratio of the kinetic energy conserved during the contact) as in Bergantz et al. (2015). Fluid and particle properties are indicated in Table 2 and taken from Michioka and Sumita (2005).

Fig. 3 shows snapshots of the particle positions for the three runs 1A–C. Particle position maps show a clear difference between simulations 1A and 1B (Fig. 3). Run 1C presents a dynamics that is intermediate between those of 1A and 1B, so results of this approach to replicate lubrication forces are discussed in details in the supplementary material SE. Both simulations with (1A) and without (1B) lubrication start with the development of small Rayleigh–Taylor instabilities at the lower front of the particle bed, with a wavelength of  $\sim 3$  mm that is consistent with that observed experimentally by Michioka and Sumita (2005) (Fig. 3 A–C). A small time delay in establishing the instabilities is observed for the simulation involving lubrication, 1A, compared to that without lubrication, 1B. Once the initial small particle plumes are formed, a larger instability is generated (Fig. 3 C–E). It is initiated by pure fluid that is buoyant relative to the suspended bed penetrating the left part of the bed. This rightward sweeping motion causes en masse bed sedimentation to produce a large particle plume encompassing most of the smaller plumes already sedimenting. We tested if the domain size controls the nature of the Rayleigh–Taylor instabilities observed in the experiments by varying the domain width, and observed the same kind of en masse bed sedimentation. It is always initiated by the opening of the particle bed in positions where the crystal network presents a lower particle volume fraction compared to the average random initial condition.

All simulations display large plumes of similar shapes (Fig. 3 D–E), except that the plume of run 1A is slightly more narrow and of higher density than that of run 1B. The main effect of lubrication forces is on the duration of the development of the large instability responsible for en masse bed sedimentation. In run 1B, the large plume starts after 12 s (Fig. 3 C), and the plume reaches half of the tank height after 15 s (Fig. 3 D), whereas these steps are observed after 15 s and 18.8 s in run 1A, respectively (Fig. 3 D–E).

We selected in simulation 1A a group of neighboring particles within the large plume and tracked the time evolution of their individual relative velocities with the surrounding fluid,  $v_f$ , and of their relative velocities,  $v_p$ . The local particle volume fraction,  $\Phi$ , is computed on the continuous grid (i.e. in each fluid computational cell) and is interpolated at each particle location. For each particle, the representative velocity relative to the neighboring particles is the magnitude of the sum of all the relative velocity vectors between that particle and its neighbors. The representative incidence angle is the average of all the pairwise angles between a given particle and its neighbors. Both relative velocities,  $\beta$ , and  $\Phi$  were averaged over the group of particles and their time evolution was smoothed by performing a zero-phase moving average (Fig. 4). These smoothed parameters can be used to calculate the force balance, and Fig. 5 F shows snapshots of the locations of the selected particle group alongside their positions on the force diagram of Fig. 2.

At the start of the simulation, the particles are in a jammed state and undergo a slow dilation, as highlighted by the slight decrease of the particle volume fraction and the increase of  $v_p$  up to 12 s (Fig. 4 B). The entire bed is falling slowly under the influence of gravity without becoming deformed as shown by the constant value of  $v_f$  (Fig. 4 B) and by the pure fluid layer that forms atop the bed (Fig. 5 A). During this process, the buoyancy and drag forces felt by the particles are in



**Fig. 3.** Snapshots from simulations 1A–C after 0 s [A], 6 s [B], 12 s [C], 15 s [D], 18.8 s [E] and 25 s [F]. Snapshots [A]–[C] are truncated and snapshots [D]–[F] represent the entire simulation domain. Filled and open circles represent the particles. Black disks represent the simulation involving lubrication forces (1A). Open red circles correspond to the simulation without lubrication (1B). The green open circles represent the run mimicking lubrication by reducing the restitution coefficients (1C).

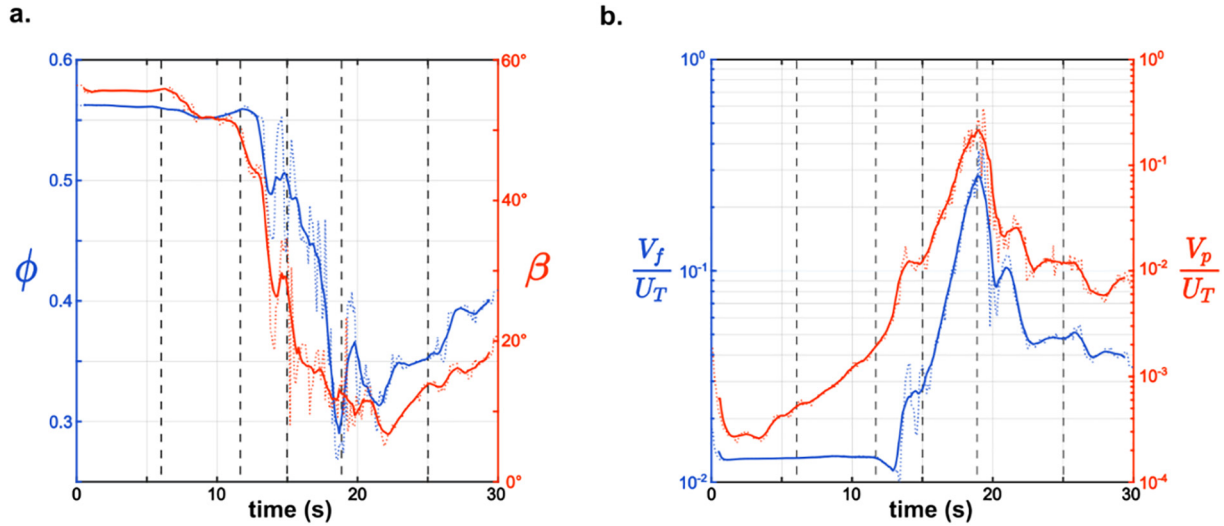


**Fig. 4.** Temporal evolution of the physical parameters encountered by the group of tracked particles. [A] The graph has two ordinate axes. The blue axis and curve represent the local particle volume fraction averaged over the group of particle,  $\phi$ . The red axis and curve represent the average incidence angle,  $\beta$ . [B] The graph has two ordinate axes. The blue axis and curve represent the ratio between the particle–fluid relative velocity and the terminal fall velocity,  $V_f/U_T$ . The red axis and curve represent the ratio between the particles edges relative velocity and the terminal fall velocity,  $V_p/U_T$ . Vertical dashed lines represent the times at which the snapshots of Fig. 3 were taken.

equilibrium (Fig. 5 F) until the bed reaches its terminal fall velocity while keeping the same shape. The buoyant fluid is thus transported by porous flow through the pack of selected particles. At 12 s, lubrication forces become dominant (Fig. 5 F) because the particle relative velocity increases while the particle volume fraction is still close to its maximum. This point also corresponds to the time when the largest

delay occurs between simulations 1A and 1B. After 15 s, when the large instability forms on the left part of the bed,  $v_f$  increases again (Fig. 4 B) and the viscous drag tends to control particles motion (Fig. 5 F). This suggests that the large plume is formed by the viscous entrainment of the fluid rather than by the net weight of the particles. During the large plume unfolding and sedimentation,  $v_p$  and  $v_f$  increase (Fig. 4

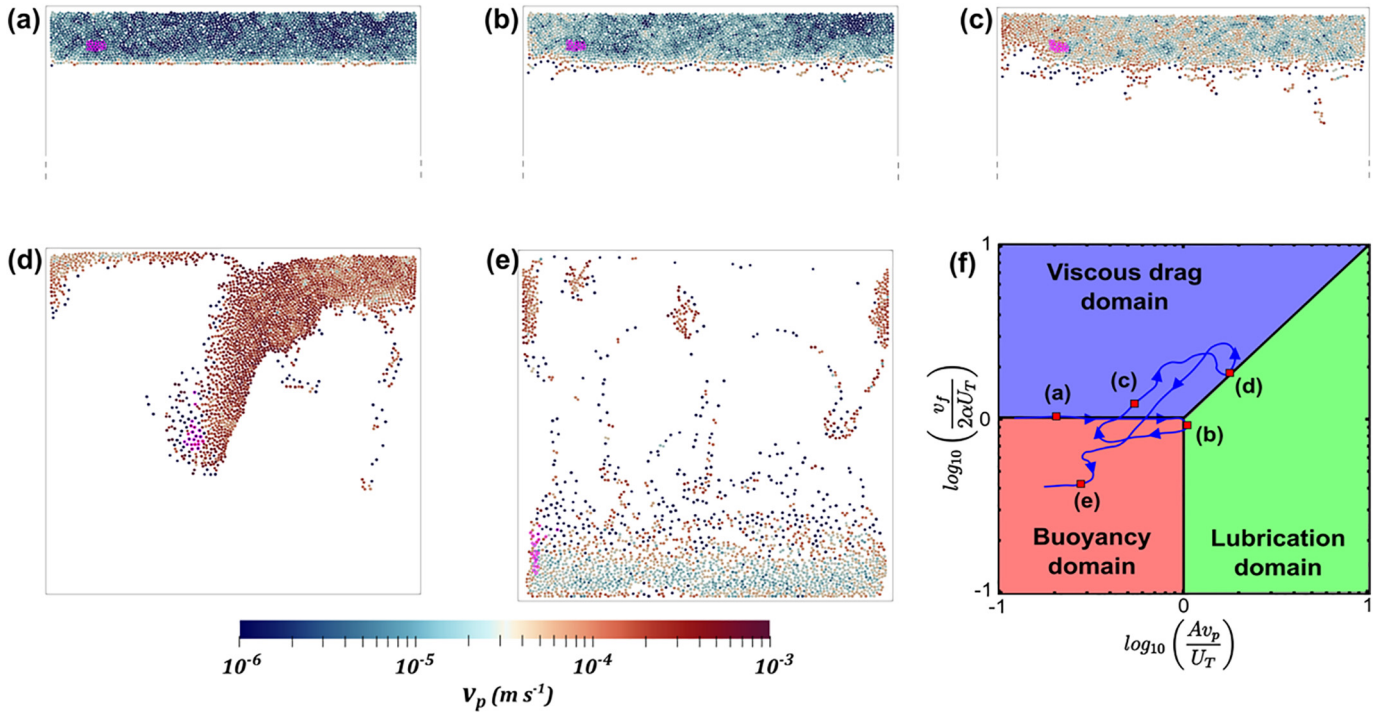


**Fig. 5.** Analysis of the results of the simulation involving lubrication (1A) with the scaling summarized in Fig. 2. Plots [A], [B], [C], [D], and [E] represent snapshots of simulation 1A after 6 s, 12 s, 15 s, 18.8 s, and 25 s, respectively. Particles are represented by disks, the color of which depends on the value of the average relative velocity between a particle and its neighbors. The group of tracked particles is indicated by purple circles. Graph [F] displays the position of the group of tracked particles on the force scaling graph. The red, blue, and green areas represent the domain where buoyancy, drag, or lubrication dominates, respectively. The positions of the tracked particles at time steps [A]–[E] are indicated by red squares and depend on the average parameters reported in Fig. 4. The blue curve represents the dynamic history of the tracked particles.

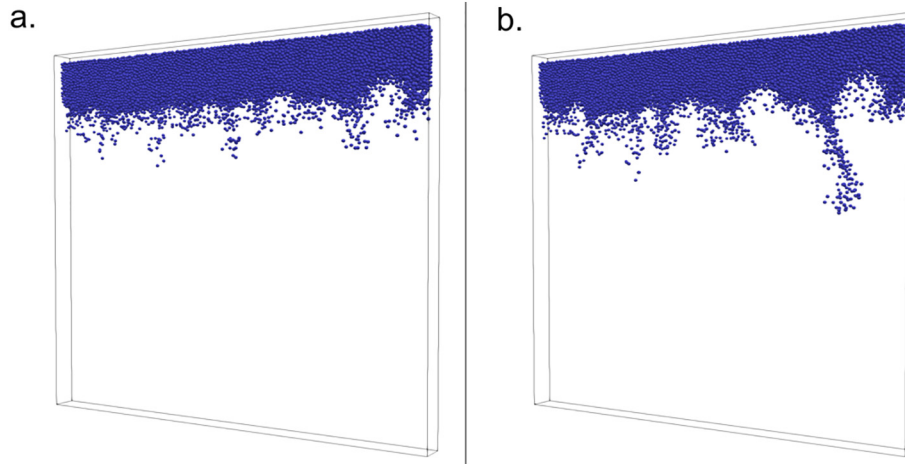


**Fig. 6.** Snapshot at identical times (22 s) of the Rayleigh-Taylor simulations 1A and 1B performed in 3D. Black lines indicate the computational domain boundaries and blue spheres are particles. [A] Run with lubrication forces. [B] Run where lubrication forces are neglected.

B) and equilibrium between fluid drag and lubrication occurs (Fig. 5 F). When the plume reaches the bottom of the tank,  $v_p$  and  $v_f$  decrease,  $\phi$  slowly increases and particle settling is controlled by their buoyancy.

Our results show a good correlation between both relative velocities after the initial bed expansion (Fig. 4 B). Furthermore,  $v_f$  and  $v_p$  appear to be inversely proportional to the local solid volume fraction (Fig. 4 A), which suggests that they are not coupled directly, but that the coupling occurs through to the local particle concentration. Decreasing particle concentration results in a joint increase of the distance between particle edges and of bed permeability. As for magmas, the characteristic Stokes numbers of the simulation are small ( $10^{-4} < St < 10^{-2}$ ), which indicates a strong coupling between fluid and particles. The relative velocity  $v_f$  is thus strongly controlled by fluid-particle drag. As particle volume fraction decreases, so does the drag force, and higher relative fluid velocities are possible within the dense suspension. The same mechanism holds for  $v_p$ , because of the monotonic relationship between lubrication forces and particle concentration. At low concentrations, particles can achieve higher relative velocities before lubrication forces dissipate the particles kinetic energy. We expect that the observed correlation between  $v_f$  and  $v_p$  breaks down for flows featuring high Stokes numbers, such as pyroclastic flows.

The 2D geometry used in these simulations has been shown to affect the results obtained by both numerical (e.g. Li et al., 2014; Peirano et al., 2001) and experimental studies on dense suspension dynamics (e.g., Courrech du Pont et al., 2003). It reduces the degrees of freedom that particles have to move relative to each other, which can potentially increase the particle relative velocities compared to the 3D case. To test the influence of the 2D geometry, we ran partial simulations of the settling runs 1A and 1B with a 3D geometry by imposing a width to the tank,  $W$ , of ten particle diameters ( $W \approx 10 d_p$ ), with the same boundary conditions as the 2D simulations. Fig. 6 displays snapshots of these simulations captured after 22 s of sedimentation. The 3D results do not exhibit the en masse bed sedimentation associated with the formation of a large plume that characterizes the 2D simulations. Sedimentation is instead characterized by multiple thinner plumes, which is more consistent with the experimental results of Michioka and Sumita (2005). This is probably due to the third spatial dimension involved, which smooths the local particle volume fraction and hinders the emergence

of the fluid-rich gaps that characterize 2D simulations. The time delay observed between the run involving lubrication (Fig. 6 A) and the one neglecting it (Fig. 6 B) is less pronounced than the lag observed with the 2D simulations. This suggests that the effect of lubrication forces is overestimated with a 2D geometry.

### 3.2.2. Experiment 2: injection of a fresh magma into a magmatic mush

Previous studies (Bergantz et al., 2017, 2015; Schleicher et al., 2016; Schleicher and Bergantz, 2017) have shown that the local injection of a crystal-free magma inside a mush produces a localized fluidized area delimited by soft faults called the mixing bowl where mixing between injected and resident melts occurs within the resident crystal cargo. To test the role of lubrication forces in such a situation, we performed numerical simulations that keep the same particle and fluid properties these authors used (see Table 3). The dimensions of the bed and injection width were, however, reduced to limit computation duration. We conserved the same ratio between the injection velocity,  $U_{inj}$ , and the minimum fluidization velocity,  $U_{mf}$ , predicted by (Cui et al., 2014) as the one they used ( $U_{inj} = 9.3 U_{mf}$ ). We performed two simulations that are summarized in Table 3. Simulation 2A took into account both normal and tangential lubrication forces. Simulation 2B did not involve lubrication, and thus corresponds to the original case explored by Bergantz et al. (2015) with higher coefficients of restitution. Two additional simulations that mimic lubrication by using low restitution coefficients identical to those of Bergantz et al. (2015) have a behavior intermediate to those of 2A and 2B and are discussed in details in the supplementary material SIE.

Overall, simulations 2A and 2B exhibit the same kind of differences as observed in experiment 1. Both runs have very similar kinematics and dynamics during the ascent of the injected magma. They both start with the initial growth of a cavity just above the inlet. We did not observe any difference between the simulations up to this point. An instability then forms at the top of the cavity once the cavity area is large enough, and the cavity rises through the mush. Fig. 7 displays snapshots of the simulations after 9.8 s of injection when the cavity reaches the top of the bed in run 2B. Each simulation ends with the establishment of a pulsating quasi-steady chimney between two counter-rotating 'granular vortices'. Run 2A presents a delay compared to run 2B

**Table 3**

Parameters used for the simulations involving the injection of crystal-free basalt inside a basaltic mush.

Run	$\eta_f$ (Pa s)	$d_p$ (m)	$\rho_p$ (kg m <sup>-3</sup> )	$\rho_f$ (kg m <sup>-3</sup> )	Bed size (m × m)	$e_n$	$e_t$	Injection width (m)	Injection velocity (m s <sup>-1</sup> )	Lubrication
2A	0.2	$4 \pm 0.2 \cdot 10^{-3}$	3300	2650	$0.96 \times 0.40$	0.7	0.35	0.16	0.023	Yes
2B	0.2	$4 \pm 0.2 \cdot 10^{-3}$	3300	2650	$0.96 \times 0.40$	0.7	0.35	0.16	0.023	No

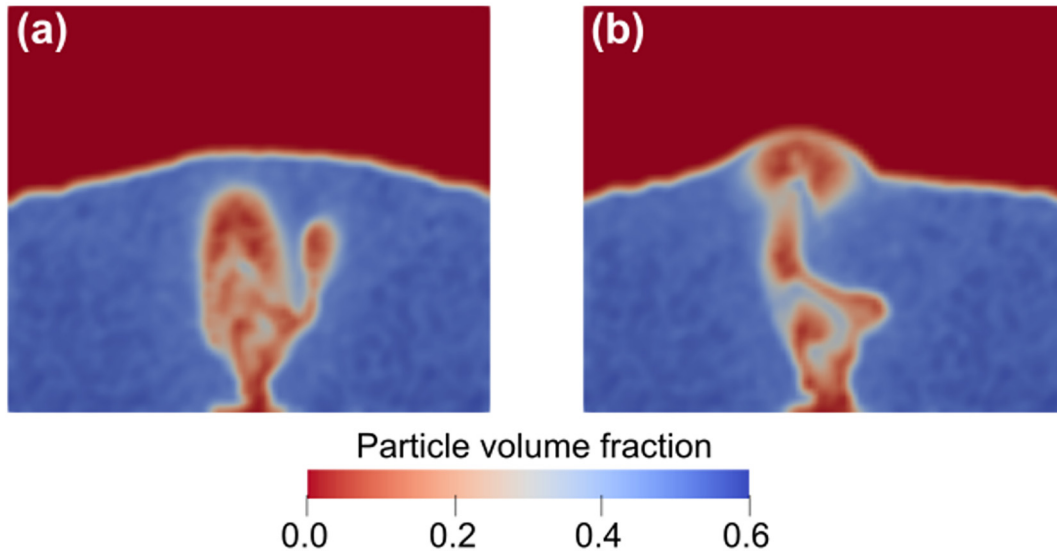


**Fig. 7.** Snapshots of experiment 2 simulations. All simulations are displayed at the same time step, after 9.8 s of injection. The color code indicates the local particle volume fraction, which is in blue at its maximum and red when the cell only contains fluid. [A] Simulation involving lubrication (2A). [B] Simulation without lubrication (2B).

because of lubrication forces (Fig. 7 A–B). The delay between runs 2A and 2B increases during the rise of the unstable cavity within the mush. An accumulated time difference of 1.1 s is observed between the two simulations when the injected magma reaches the top of the mush bed.

### 3.3. Interpretation

Fig. 2 shows that the scaling relationships we propose can discriminate under which conditions lubrication forces are important. Their importance in controlling the dynamics of a dense suspension depends on the interplay of hydrodynamic stress exerted by the carrier phase, the velocity fluctuations among the solids, and the local particle concentration. The importance of drag and lubrication forces are inversely proportional to  $S_T$  and  $S_O$ , respectively. In general, when  $S_T \ll 1$  and  $S_O \ll 1$ , the buoyancy force is negligible. This is usually the case for magmatic mixtures, which are characterized by high viscosities and small crystal sizes. The relative importance of lubrication forces over the drag force is expressed in the ratios  $S_T/S_O$  and  $\tilde{v}_p/\tilde{v}_f$ . Our simulations show that  $\tilde{v}_p$  and  $\tilde{v}_f$  coevolve when  $S_T \ll 1$ , and that  $\sim 0.1 < \tilde{v}_p/\tilde{v}_f < \sim 1$  (Fig. 4 B). This ratio does not vary significantly with the particle volume fraction. On the contrary, the ratio  $S_T/S_O$  depends on the particle volume fraction and tends to infinity when approaching maximum packing. The ratio  $S_T \tilde{v}_p/S_O \tilde{v}_f$  is equal to  $2\alpha A \frac{\tilde{v}_p}{\tilde{v}_f}$ , which is a function of the solid concentration and the incidence angle  $\beta$ . Fig. 8 displays curves of critical particle concentrations at which the transition between dynamics dominated by the drag or lubrication forces occurs ( $S_T \tilde{v}_p/S_O \tilde{v}_f = 1$ ). Above the critical concentration, lubrication forces have a larger magnitude than the drag force, and produce an apparent strain hardening at the onset, or at the end, of motion within the crystal network. Below the critical concentration, lubrication forces have a lower magnitude than the drag force and have only a marginal effect on dynamics as highlighted in our simulations (Fig. 3).

## 4. Discussion

### 4.1. Influence of crystal size and shape polydispersity

We represent crystals as spheres with a unimodal size distribution. This is not the case in magmatic systems, where crystal size

distributions (CSD) are polydisperse and often polymodal, and crystals are not spherical (Higgins, 2006; Higgins and Roberge, 2003; Marsh, 1988; Picard et al., 2011). The particle aspect ratio affects the rheology of crystal-bearing magmas (Cimarelli et al., 2011; Mueller et al., 2011, 2010; Picard et al., 2011; Mader et al., 2013; Moitra and Gonnermann, 2015). Both drag and lubrication forces become non-uniform around the crystals and depend on the orientations of the elongated particles (Bergantz et al., 2017). The relationship between particle shape and drag also influences their terminal fall velocity (Dellino et al., 2005). This last effect can be added into the numerical simulations by introducing a shape factor on the drag expression (Dioguardi et al., 2014). Some methods also exist to incorporate the particles shape within lubrication expressions, but they require additional iterations to find the minimum gap position and principal curvature direction between two elongated particles (Claeys and Brady, 1993; Janoschek et al., 2013). This

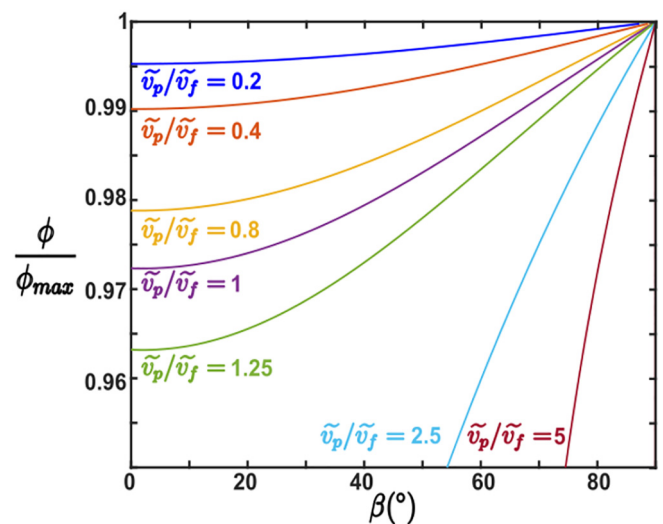


**Fig. 8.** Evolution of the critical relative particle concentration as functions of the angle  $\beta$  and the ratio  $\tilde{v}_p/\tilde{v}_f$ . All curves correspond to the values of the critical concentration at which  $S_T \tilde{v}_p/S_O \tilde{v}_f = 1$ . Their colors depend of the imposed ratio  $\tilde{v}_p/\tilde{v}_f$ . Each curve presents a minimum critical concentration when the relative motion of the particle is nearly normal ( $\beta \rightarrow 0$ ), and a maximum at a relative particle concentration of  $\sim 1$  when the relative motion is purely tangential ( $\beta = 90^\circ$ ).

calculation needs to be performed at each DEM time step and for each particle pair, which increases the computational cost of the simulations. Contact forces are not included within our scaling but are nevertheless present in nature and within the simulations. For non-spherical particles, the contact torques between non-spherical particles depend on the contact position and orientation (Bergantz et al., 2017). Our results and conclusions are therefore valid for spherical particles and are to be extended with caution to natural systems.

We employed three distinct but close particle sizes in order to avoid artificial shape ‘crystallization’. This cannot be viewed as representative of the polydispersity present in natural systems. The CSD is an important parameter that controls the dynamic of the particles because each force and dimensionless number we considered depends on particle diameter. CSD also affects the maximum packing fraction that a dense suspension can reach. Maximum packing increases when the suspension is polydisperse, and, Apollonian packing aside, it is maximal when the CSD is bimodal with ~25% of fine particles and ~75% coarse particles (Ouchiyama and Tanaka, 2002; Farr and Groot, 2009; Faroughi and Huber, 2014). The effect of polydispersity on the force balance is not obvious because a high degree of polydispersity decreases particle bed permeability but increases the coordination number and thus the number density of lubricated bridges.

#### 4.2. Comparison with other studies

Relationships exist to scale the competition between lubrication and friction in dense suspensions (Coussot and Ancey, 1999; Fernandez et al., 2013; Ness and Sun, 2015). These works motivated Bergantz et al. (2017) to scale the transition between dynamic regimes dominated by either friction or lubrication in magmas (we call here the dimensionless number characterizing the lubrication/friction transition the Leighton number,  $Le$ , to distinguish it from the Sommerfeld number we propose). At low  $Le$ , particles are in direct contact and at large  $Le$ , particles are separated by a lubrication film. This number is proportional to the distance between particle edges and fails to properly measure the importance of lubrication when particles tend to be far away from each other (Fernandez et al., 2013). It is thus unable to capture the transition between dynamic regimes where crystal motions are governed by either the lubricated film or melt motions that are further afield. In our formulation, however, lubrication is inversely proportional to  $S_0$  and to the distance between the particles. It thus properly scales the transition between lubricated and hydrodynamic regimes but fails to predict the onset of frictional behavior. The two scaling numbers are thus complementary to describe all the regime transitions that can be encountered in magmatic mush.

Our observations on the effect of lubrication on the macroscopic dynamics of a magmatic mush fit well with the results of Mutabaruka et al. (2014) on the initiation of motion in immersed granular avalanche. They observed the formation of a strain hardening followed by relaxation associated with dilation of the solid network when the initial particle concentration tends towards its maximum. At the initiation of the granular avalanche, they observed bed expansion when the initial particle concentration is higher than ~0.59. This corresponds to ratios  $\Phi/\Phi_{max} > 0.92$  with  $\Phi_{max} = 0.64$ . This illustrates well the importance of lubrication forces at the onset of motion of dense suspensions.

#### 4.3. Implication on magma rheology and magmatic system dynamics

As in our experiments, magmatic mixtures are characterized by low Stokes numbers,  $S_T \ll 1$ , which indicates strong coupling between crystals and melt (Burgisser et al., 2005). Because of this dynamic similarity, we expect that our simulations illuminate the role of lubrication forces on mush dynamics and rheology. The rheology of magmas and mushes is now often studied by shearing or uniaxial compression experiments under high temperature and high confining pressure (e.g. Caricchi et al., 2007; Champallier et al., 2008; Laumonier et al., 2014, 2013;

Lavallée et al., 2013, 2007). Capturing lubrication in such experiments, however, is challenging for several reasons. Our results show that lubrication effects appear when the crystal network is free to expand in response to deformation. Experiments involving water-bearing melts (e.g., Caricchi et al., 2007), however, feature a metal jacket that encloses the sample and prevents such dilation. This suggests that jacket-free experiments typical of uniaxial apparatus (e.g., Lavallée et al., 2007) have better chances to evidence lubrication. Bulk viscosities are determined using experimental data acquired when an apparent steady state is reached, which leaves out the initial transient response to the imposed constraint. Our results show that lubrication forces under quasi-steady state are weaker than other hydrodynamic micro-scale processes. It is not the case, however, when deformation is transient. This suggests that lubrication could be captured in shearing or compression experiments performed on samples near maximum packing during the initiation of shearing or during an abrupt change of the imposed shear rate. Initial non-linear increases in the stresses and apparent viscosities are well documented (Caricchi et al., 2007; Champallier et al., 2008; Lavallée et al., 2007). As these effects are observed for all particle concentrations (Champallier et al., 2008), they are inferred to reflect the combined effects of the elastic response of the experimental apparatus and of the initial reorganization of the particles in the pre-compacted sample (Lavallée et al., 2007). Our results suggest that these early non-linear stress responses and those following changes in applied strain rates might contain yet unexploited information on lubrication.

To identify which degrees of freedom control lubrication under magmatic conditions, we performed a Monte-Carlo analysis by varying the variables present in Eq. (1) over possible ranges encountered in magmas and mushes (Table 4). Fig. 9 A displays the results in a format that recovers the same phase-space as that of Fig. 2. We report in Fig. 9 B–F the probability density distribution of the variables involved in the realizations where lubrication is the dominant force. Lubrication effects are expected to appear more often with small crystals rather than large ones (Fig. 9 B). It is not surprising because lubrication forces depend linearly on crystal diameter whereas the terminal velocity depends on the square of it (Eq. (5)). The dependence on the melt viscosity shows that highly viscous melt are more likely to be in lubricated conditions (Fig. 9 C). As expected from our scaling, the two main parameters that control the importance of lubrication are the relative velocities between the crystals and the surrounding melt (Fig. 9 D and F). These two parameters may be very difficult to measure during experiments on magma rheology as they are dynamical properties. This is a reminder that the rheology of magmas and mushes depends greatly on such dynamic properties in addition to materials properties, which are the only ones often reported and used in studies treating magma rheology as a single fluid. The relative velocities between crystals and melt affects the time crystals have to respond to changes in chemical environment during mush unlocking. Owing to experimental limitations and to the strong tendency that multiphase suspensions have to foster particle gathering and dispersal when subjected to shear, such transient motions are difficult to appraise. Their understanding is nevertheless

**Table 4**

Parameter ranges used for the Monte-Carlo analysis. Ranges were chosen to represent possible conditions encountered in magmatic systems while remaining in the validity domain of our analysis.

Parameter	Lower bound	Upper bound
$\rho_p$ (kg m <sup>-3</sup> )	2700	3300
$\rho_f$ (kg m <sup>-3</sup> )	2450	3300
$d_p$ (m)	10 <sup>-4</sup>	5.10 <sup>-3</sup>
$\eta_f$ (Pa s)	10 <sup>1</sup>	10 <sup>4</sup>
$\varphi/\varphi_{max}$	0.5	0.99999
$\beta$ (°)	0	90
$v_p$ (m s <sup>-1</sup> )	10 <sup>-6</sup>	10 <sup>-1</sup>
$v_f$ (m s <sup>-1</sup> )	10 <sup>-6</sup>	10 <sup>-1</sup>

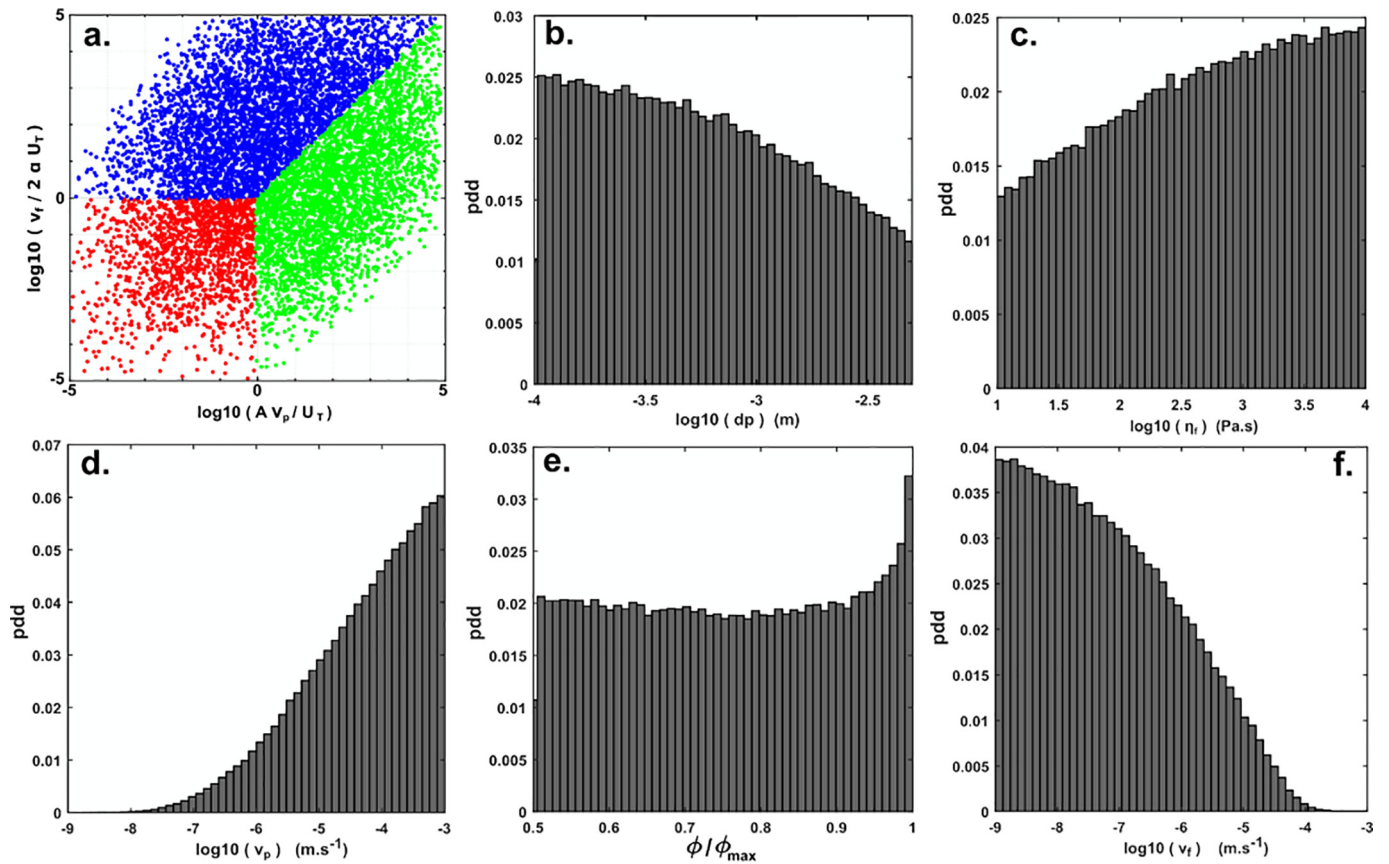


**Fig. 9.** Exploration of the importance of lubrication in magmatic context. (a). Results of the Monte-Carlo analysis. Results are reported on logarithmic scales with the ratios  $A v_p / U_T$  as abscissa and  $v_f / 2 \alpha U_T$  as ordinate. We report only  $10^4$  of the  $10^6$  total realizations for clarity. Each dot corresponds to a realization and its color depends on the force with the highest magnitude. Realizations dominated by buoyancy, drag, or lubrication are indicated by red, blue, or green dots, respectively. [B–F] Probability density distributions (pdd) of the parameters involved in realizations where the lubrication forces dominate the others. We only reported the distributions of crystal diameter [B], fluid viscosity [C], particle relative velocity [D], the ratio of the particle volume fraction [E], and the relative velocity between the particle and the fluid [F].

crucial to fully describe magma rheology and to predict the rate and duration of dynamic remobilization processes within magmatic systems.

Silicic magma bodies are thought to be formed by several increments of injected magma (Annen and Sparks, 2002) that cool, degas, and crystallize to reach a mushy state (Bachmann and Bergantz, 2004). In such systems, several scenarios have been evoked to explain eruption triggering. One is the rejuvenation of the magmatic mush associated with the injection of crystal-poor magmas (e.g. Pallister et al., 1992; Tomiya and Takeuchi, 2009). Another is the reactivation of the magmatic mush resulting from the emplacement of a hot batch of magma at the base of the crystal mush, which heats it up and melts the mush crystals to produce a mobile layer that eventually becomes unstable and ascends through the mush (Burgisser and Bergantz, 2011). Yet another scenario is crustal faulting that causes deep fragmentation of mush materials (Gottsmann et al., 2009). Each of these scenarios requires the initiation of motion within the mush. Our simulations have shown that lubrication forces produce strain hardening followed by softening during such event. These forces likely play an important role in controlling the ascent rates and timescales of magmas within the crust. Neglecting them could result in underestimating the resistance of the mush to the arrival of mobile magma. For instance, a magma batch ascending through a mush needs to continuously initiate the motion of the overlying crystals in order to open and penetrate the mush. Lubrication forces are opposed to this process and therefore slow down the ascent of the magma batch. In addition, the ascending magma batch is expected to form a fluidized chimney in its wake (e.g. Girard and Stix, 2009). Our results show that lubrication forces are important

when the crystal-bearing magma is approaching jamming, a result consistent with other numerical and experimental results. These forces oppose the closing and clogging of the fluidized chimney, which tends to maintain the feeding system of the ascending batch. The overall effect of lubrication forces on such phenomena is thus a complex combination of both effects that needs further exploration because it bears on our capability to accurately predict timescales of magmatic mushes dynamics.

## 5. Conclusions

Using numerical simulation, we demonstrate that lubrication forces cannot be neglected when a magmatic mush exits or enters a jammed state. Our numerical experiments of sedimentation and remobilization of packed particle beds notably show that an apparent bulk strain hardening is produced by lubrication forces, which results in belated dynamics. We propose scaling relationships that highlight the dominant role of lubrication forces as the cause of the strain hardening and softening observed. This scaling leads us to propose a new formulation of the Sommerfeld number to scale the transition between hydrodynamic and lubricated regimes. Our formulation is complementary to that previously used in the literature aimed at capturing the transition between frictional and lubricated regimes. The two formulations can predict the overall transitions in dynamic regimes that a magmatic mush can be subjected to. Understanding lubrication has implications on the timescales of magmatic mush processes that control crystal thermal histories.

## Acknowledgments

All the numerical simulations presented in this paper were performed using the CIMENT infrastructure (<https://ciment.ujf-grenoble.fr>), which is supported by the Rhône-Alpes region (GRANT CPER07\_13 CIRA: <http://www.ci-ra.org>). This manuscript greatly benefits from the helpful reviews and comments from Yan Lavallee and an anonymous reviewer. A.C. and A.B. were partially funded by a grant from Labex OSUG@2020 (Investissements d'avenir – ANR10 LABX56), grant A07bis-International 2017 and grant ChaMaFo from the University Savoie Mont Blanc. G.W.B. was supported by National Science Foundation grants DGE-1256068, EAR-1049884 and EAR-1447266. Authors declare no conflicts of interest.

## Appendix A. Supplementary data

Supplementary data to this article can be found online at <https://doi.org/10.1016/j.jvolgeores.2019.05.008>.

## References

- Ancey, C., Coussot, P., Evesque, P., 1999. A theoretical framework for granular suspensions in a steady simple shear flow. *J. Rheol.* 43, 1673–1699. <https://doi.org/10.1122/1.551067>.
- Andreotti, B., Forterre, Y., Pouliquen, O., 2013. *Granular Media: Between Fluid and Solid*. Cambridge University Press.
- Annen, C., Sparks, R.S.J., 2002. Effects of repetitive emplacement of basaltic intrusions on thermal evolution and melt generation in the crust. *Earth Planet. Sci. Lett.* 203, 937–955. [https://doi.org/10.1016/S0012-821X\(02\)00929-9](https://doi.org/10.1016/S0012-821X(02)00929-9).
- Bachmann, O., Bergantz, G.W., 2004. On the origin of crystal-poor rhyolites: extracted from batholithic crystal mushes. *J. Petrol.* 45, 1565–1582.
- Barboni, M., Boehnke, P., Schmitt, A.K., Harrison, T.M., Shane, P., Bouvier, A.-S., Baumgartner, L., 2016. Warm storage for arc magmas. *Proc. Natl. Acad. Sci.* 201616129. <https://doi.org/10.1073/pnas.1616129113>.
- Bergantz, G.W., Ni, J., 1999. A numerical study of sedimentation by dripping instabilities in viscous fluids. *Int. J. Multiph. Flow* 25, 307–320. [https://doi.org/10.1016/S0301-9322\(98\)00050-0](https://doi.org/10.1016/S0301-9322(98)00050-0).
- Bergantz, G.W., Schleicher, J.M., Burgisser, A., 2015. Open-system dynamics and mixing in magma mushes. *Nat. Geosci.* 8, 793–796. <https://doi.org/10.1038/ngeo2534>.
- Bergantz, G.W., Schleicher, J.M., Burgisser, A., 2017. On the kinematics and dynamics of crystal-rich systems. *J. Geophys. Res. Solid Earth* 122. <https://doi.org/10.1002/2017JB014218>.
- Burgisser, A., Bergantz, G.W., 2011. A rapid mechanism to remobilize and homogenize highly crystalline magma bodies. *Nature* 471, 212–215. <https://doi.org/10.1038/nature09799>.
- Burgisser, A., Bergantz, G.W., Breidenthal, R.E., 2005. Addressing complexity in laboratory experiments: the scaling of dilute multiphase flows in magmatic systems. *J. Volcanol. Geotherm. Res.* 141, 245–265. <https://doi.org/10.1016/j.jvolgeores.2004.11.001>.
- Caricchi, L., Burlini, L., Ulmer, P., Gerya, T., Vassalli, M., Papale, P., 2007. Non-Newtonian rheology of crystal-bearing magmas and implications for magma ascent dynamics. *Earth Planet. Sci. Lett.* 264, 402–419. <https://doi.org/10.1016/j.epsl.2007.09.032>.
- Cashman, K.V., Sparks, R.S.J., Blundy, J.D., 2017. Vertically extensive and unstable magmatic systems: a unified view of igneous processes. *Science* 355, eaag3055. <https://doi.org/10.1126/science.aag3055>.
- Champallier, R., Bystricky, M., Arbaret, L., 2008. Experimental investigation of magma rheology at 300 MPa: from pure hydrous melt to 76 vol.% of crystals. *Earth Planet. Sci. Lett.* 267, 571–583. <https://doi.org/10.1016/j.epsl.2007.11.065>.
- Chen, X., Wang, J., 2014. A comparison of two-fluid model, dense discrete particle model and CFD-DEM method for modeling impinging gas–solid flows. *Powder Technol.* 254, 94–102. <https://doi.org/10.1016/j.powtec.2013.12.056>.
- Cimarelli, C., Costa, A., Mueller, S., Mader, H.M., 2011. Rheology of magmas with bimodal crystal size and shape distributions: Insights from analog experiments. *Geochem. Geophys. Geosystems* 12. <https://doi.org/10.1029/2011GC003606>.
- Claeys, L.L., Brady, J.F., 1993. Suspensions of prolate spheroids in Stokes flow. Part 1. Dynamics of a finite number of particles in an unbounded fluid. *J. Fluid Mech.* 251, 411–442. <https://doi.org/10.1017/S0022112093003465>.
- Cooper, K.M., Kent, A.J.R., 2014. Rapid remobilization of magma crystals kept in cold storage. *Nature* 506, 480–483.
- Cordonnier, B., Caricchi, L., Pistone, M., Castro, J., Hess, K.-U., Gottschaller, S., Manga, M., Dingwell, D.B., Burlini, L., 2012. The viscous-brittle transition of crystal-bearing silicic melt: direct observation of magma rupture and healing. *Geology* 40, 611–614. <https://doi.org/10.1130/G3914.1>.
- Courrech du Pont, S., Gondret, P., Perrin, B., Rabaud, M., 2003. Wall effects on granular heap stability. *EPL Europhys. Lett.* 61, 492. <https://doi.org/10.1209/epl/i2003-00156-5>.
- Coussot, P., Ancey, C., 1999. Rheophysical classification of concentrated suspensions and granular pastes. *Phys. Rev. E* 59, 4445–4457. <https://doi.org/10.1103/PhysRevE.59.4445>.
- Cui, X., Li, J., Chan, A., Chapman, D., 2014. Coupled DEM–LBM simulation of internal fluidisation induced by a leaking pipe. *Powder Technol.* 254, 299–306. <https://doi.org/10.1016/j.powtec.2014.01.048>.
- Deen, N.G., Annaland, M. van S., Hoef, M.A. van der, Kuipers, J.A.M., 2007. Review of discrete particle modeling of fluidized beds. *Chem. Eng. Sci.* 62, 28–44. <https://doi.org/10.1016/j.ces.2006.08.014>.
- Dellino, P., Mele, D., Bonasia, R., Braia, G., Volpe, L.L., Sulpizio, R., 2005. The analysis of the influence of pumice shape on its terminal velocity. *Geophys. Res. Lett.* 32. <https://doi.org/10.1029/2005GL023954>.
- Dioguardi, F., Dellino, P., Mele, D., 2014. Integration of a new shape-dependent particle–fluid drag coefficient law in the multiphase Eulerian–Lagrangian code MFX-DEM. *Powder Technol.* 260, 68–77. <https://doi.org/10.1016/j.powtec.2014.03.071>.
- Faroughi, S.A., Huber, C., 2014. Crowding-based rheological model for suspensions of rigid bimodal-sized particles with interfering size ratios. *Phys. Rev. E* 90, 052303.
- Farr, R.S., Groot, R.D., 2009. Close packing density of polydisperse hard spheres. *J. Chem. Phys.* 131, 244101.
- Fernandez, N., Mani, R., Rinaldi, D., Kadau, D., Mosquet, M., Lombois-Burger, H., Cayer-Barrois, J., Herrmann, H.J., Spencer, N.D., Isa, L., 2013. Microscopic mechanism for shear thickening of non-Brownian suspensions. *Phys. Rev. Lett.* 111, 108301. <https://doi.org/10.1103/PhysRevLett.111.108301>.
- Frankel, N.A., Acrivos, A., 1967. On the viscosity of a concentrated suspension of solid spheres. *Chem. Eng. Sci.* 22, 847–853. [https://doi.org/10.1016/0009-2509\(67\)80149-0](https://doi.org/10.1016/0009-2509(67)80149-0).
- Garg, R., Galvin, J., Li, T., Pannala, S., 2010. Documentation of Open-source MFX-DEM Software for Gas-solids Flows (URL [Httpsmfx.Netl.Doe.Govdocumentationdemdoc2012-1.Pdf](http://Httpsmfx.Netl.Doe.Govdocumentationdemdoc2012-1.Pdf) Accessed 31 March 2014).
- Garg, R., Galvin, J., Li, T., Pannala, S., 2012. Open-source MFX-DEM software for gas–solids flows: part I—verification studies. *Powder Technol.* 220, 122–137.
- Girard, G., Stix, J., 2009. Buoyant replenishment in silicic magma reservoirs: experimental approach and implications for magma dynamics, crystal mush remobilization, and eruption. *J. Geophys. Res. Solid Earth* 114, B08203. <https://doi.org/10.1029/2008JB005791>.
- Gondret, P., Lance, M., Petit, L., 2002. Bouncing motion of spherical particles in fluids. *Phys. Fluids* 14, 643–652. <https://doi.org/10.1063/1.1427920>.
- Gottsmann, J., Lavallée, Y., Martí, J., Aguirre-Díaz, G., 2009. Magma–tectonic interaction and the eruption of silicic batholiths. *Earth Planet. Sci. Lett.* 284, 426–434. <https://doi.org/10.1016/j.epsl.2009.05.008>.
- Higgins, M.D., 2006. Verification of ideal semi-logarithmic, lognormal or fractal crystal size distributions from 2D datasets. *J. Volcanol. Geotherm. Res., Modern Trends Petrography* 154, 8–16. <https://doi.org/10.1016/j.jvolgeores.2005.09.015>.
- Higgins, M.D., Roberge, J., 2003. Crystal size distribution of plagioclase and amphibole from Soufrière Hills Volcano, Montserrat: evidence for dynamic crystallization–textural coarsening cycles. *J. Petrol.* 44, 1401–1411. <https://doi.org/10.1093/petrology/44.8.1401>.
- Hildreth, W., 2004. Volcanological perspectives on Long Valley, Mammoth Mountain, and Mono Craters: several contiguous but discrete systems. *J. Volcanol. Geotherm. Res.* 136, 169–198.
- Janoschek, F., Harting, J., Toschi, F., 2013. Accurate Lubrication Corrections for Spherical and Non-spherical Particles in Discretized Fluid Simulations (ArXiv13086482 Cond-Mat Physicsphysics).
- Jeffrey, D.J., Onishi, Y., 1984. The forces and couples acting on two nearly touching spheres in low-Reynolds-number flow. *Z. Für Angew. Math. Phys. ZAMP* 35, 634–641. <https://doi.org/10.1007/BF00952109>.
- Karlstrom, L., Rudolph, M.L., Manga, M., 2012. Caldera size modulated by the yield stress within a crystal-rich magma reservoir. *Nat. Geosci.* 5, 402–405.
- Kendrick, J.E., Lavallée, Y., Hess, K.-U., Heap, M.J., Gaunt, H.E., Meredith, P.G., Dingwell, D.B., 2013. Tracking the permeable porous network during strain-dependent magmatic flow. *J. Volcanol. Geotherm. Res.* 260, 117–126. <https://doi.org/10.1016/j.jvolgeores.2013.05.012>.
- Laumonier, M., Scaillet, B., Pichavant, M., Champallier, R., Andújar, J., Arbaret, L., 2013. On the conditions of magma mixing and its bearing on andesite production in the crust. *Nat. Commun.* 5. <https://doi.org/10.1038/ncomms6607> 12 p.
- Laumonier, M., Scaillet, B., Arbaret, L., Champallier, R., 2014. Experimental simulation of magma mixing at high pressure. *Lithos* 196–197, 281–300. <https://doi.org/10.1016/j.lithos.2014.02.016>.
- Lavallée, Y., Hess, K.-U., Cordonnier, B., Dingwell, D.B., 2007. Non-Newtonian rheological law for highly crystalline dome lavas. *Geology* 35, 843–846. <https://doi.org/10.1130/G23594A.1>.
- Lavallée, Y., Varley, N., Alatorre-Ibargüenito, M., Hess, K.-U., Kueppers, U., Mueller, S., Richard, D., Scheu, B., Spieler, O., Dingwell, D., 2012. Magmatic architecture of dome-building eruptions at Volcán de Colima, Mexico. *Bull. Volcanol.* 74, 249–260.
- Lavallée, Y., Benson, P.M., Heap, M.J., Hess, K.-U., Flaws, A., Schillinger, B., Meredith, P.G., Dingwell, D.B., 2013. Reconstructing magma failure and the degassing network of dome-building eruptions. *Geology* 41, 515–518. <https://doi.org/10.1130/G33948.1>.
- Li, T., Garg, R., Galvin, J., Pannala, S., 2012. Open-source MFX-DEM software for gas–solids flows: part II—validation studies. *Powder Technol.* 220, 138–150.
- Li, T., Pannala, S., Shahnam, M., 2014. Reprint of “CFD simulations of circulating fluidized bed risers, part II, evaluation of differences between 2D and 3D simulations”. *Powder Technol.* 265, 13–22. <https://doi.org/10.1016/j.powtec.2014.04.007> Selected Papers from the 2012 NETL Multiphase Flow Workshop.
- MacDonald, M.J., Chu, C.-F., Guilloit, P.P., Ng, K.M., 1991. A generalized Blake-Kozeny equation for multized spherical particles. *AIChE J.* 37, 1583–1588.
- Mader, H.M., Llewellyn, E.W., Mueller, S.P., 2013. The rheology of two-phase magmas: a review and analysis. *J. Volcanol. Geotherm. Res.* 257, 135–158. <https://doi.org/10.1016/j.jvolgeores.2013.02.014>.

- Mari, R., Seto, R., Morris, J.F., Denn, M.M., 2014. Shear thickening, frictionless and frictional rheologies in non-Brownian suspensions. *J. Rheol.* 58, 1693–1724. <https://doi.org/10.1122/1.4890747>.
- Marsh, B.D., 1988. Crystal size distribution (CSD) in rocks and the kinetics and dynamics of crystallization. *Contrib. Mineral. Petrol.* 99, 277–291. <https://doi.org/10.1007/BF00375362>.
- Marzougui, D., Chareyre, B., Chauchat, J., 2015. Microscopic origins of shear stress in dense fluid–grain mixtures. *Granul. Matter* 17, 297–309. <https://doi.org/10.1007/s10035-015-0560-6>.
- McIntire, Michael Z., Bergantz, George W., Schleicher, Jillian M., 2019. On the hydrodynamics of crystal clustering. *Philos. Trans. R. Soc. Math. Phys. Eng. Sci.* 377, 20180015. <https://doi.org/10.1098/rsta.2018.0015>.
- Michioka, H., Sumita, 2005. Rayleigh–Taylor instability of a particle packed viscous fluid: implications for a solidifying magma. *Geophys. Res. Lett.*, 32 <https://doi.org/10.1029/2004GL021827>.
- Moitra, P., Gonnermann, H.M., 2015. Effects of crystal shape- and size-modality on magma rheology. *Geochem. Geophys. Geosystems* 16, 1–26. <https://doi.org/10.1002/2014GC005554>.
- Mueller, S., Llewellyn, E.W., Mader, H.M., 2010. The rheology of suspensions of solid particles. *Proc. R. Soc. Lond. Math. Phys. Eng. Sci.* 466, 1201–1228. <https://doi.org/10.1098/rspa.2009.0445>.
- Mueller, S., Llewellyn, E.W., Mader, H.M., 2011. The effect of particle shape on suspension viscosity and implications for magmatic flows. *Geophys. Res. Lett.* 38. <https://doi.org/10.1029/2011GL047167>.
- Mutabaruka, P., Delenne, J.-Y., Soga, K., Radjai, F., 2014. Initiation of immersed granular avalanches. *Phys. Rev. E* 89, 052203. <https://doi.org/10.1103/PhysRevE.89.052203>.
- Ness, C., Sun, J., 2015. Flow regime transitions in dense non-Brownian suspensions: rheology, microstructural characterization, and constitutive modeling. *Phys. Rev. E* 91, 012201. <https://doi.org/10.1103/PhysRevE.91.012201>.
- Ouchiya, N., Tanaka, T., 2002. Porosity Estimation for Random Packings of Spherical Particles [WWW Document]. <https://doi.org/10.1021/i100016a019>.
- Pallister, J.S., Hoblitt, R.P., Reyes, A.G., 1992. A basalt trigger for the 1991 eruptions of Pinatubo volcano? *Nature* 356, 426–428. <https://doi.org/10.1038/356426a0>.
- Peirano, E., Delloume, V., Leckner, B., 2001. Two- or three-dimensional simulations of turbulent gas–solid flows applied to fluidization. *Chem. Eng. Sci.* 56, 4787–4799. [https://doi.org/10.1016/S0009-2509\(01\)00141-5](https://doi.org/10.1016/S0009-2509(01)00141-5).
- Petford, N., 2009. Which effective viscosity? *Mineral. Mag.* 73, 167–191. <https://doi.org/10.1180/minmag.2009.073.2.167>.
- Picard, D., Arbaret, L., Pichavant, M., Champallier, R., Launeau, P., 2011. Rheology and microstructure of experimentally deformed plagioclase suspensions. *Geology* 39, 747–750. <https://doi.org/10.1130/G32217.1>.
- Ryerson, F.J., Weed, H.C., Piwinski, A.J., 1988. Rheology of subliquidus magmas: 1. Picritic compositions. *J. Geophys. Res. Solid Earth* 93, 3421–3436. <https://doi.org/10.1029/JB093iB04p03421>.
- Schleicher, J.M., Bergantz, G.W., 2017. The mechanics and temporal evolution of an open-system magmatic intrusion into a crystal-rich magma. *J. Petrol.* 58, 1059–1072. <https://doi.org/10.1093/ptrology/egx045>.
- Schleicher, J.M., Bergantz, G.W., Breidenthal, R.E., Burgisser, A., 2016. Time scales of crystal mixing in magma mushes. *Geophys. Res. Lett.* 43, 1543–1550. <https://doi.org/10.1002/2015GL067372>.
- Sparks, R.S.J., 2003. Forecasting volcanic eruptions. *Earth Planet. Sci. Lett.* 210, 1–15. [https://doi.org/10.1016/S0012-821X\(03\)00124-9](https://doi.org/10.1016/S0012-821X(03)00124-9).
- Syamlal, M., 1998. MFX Documentation Numerical Technique. EG and G Technical Services of West Virginia, Inc., Morgantown, WV (United States).
- Syamlal, M., Rogers, W., O'Brien, T.J., 1993. MFX Documentation Theory Guide. USDOE Morgantown Energy Technology Center, WV (United States).
- Tomiya, A., Takeuchi, S., 2009. Two-Stage Magma Mixing and Initial Phase of the 1667 Plinian Eruption of Tarumai Volcano. *AGU Fall Meet. Abstr* 51.